JOURNAL OF THE MECHANICAL BEHAVIOR OF BIOMEDICAL MATERIALS 14 (2012) 143–157

Available online at www.sciencedirect.com

SciVerse ScienceDirect

journal homepage: www.elsevier.com/locate/jmbbm

Research Paper

Numerical investigation of the active role of the actin cytoskeleton in the compression resistance of cells

William Ronan[a], Vikram S. Deshpande[b], Robert M. McMeeking[c], J. Patrick McGarry[a,*]

[a]Department of Mechanical and Biomedical Engineering, National University of Ireland Galway, University Road, Galway, Ireland
[b]Department of Engineering, University of Cambridge, Trumpington Street, Cambridge CB2 1PZ, UK
[c]Department of Mechanical Engineering, University of California, Santa Barbara, CA 93106-5070, USA

ARTICLE INFO

Article history:
Received 3 February 2012
Received in revised form
22 May 2012
Accepted 24 May 2012
Available online 21 June 2012

Keywords:
Stress fibre
Active contractility
Constitutive formulation
Cell compression

ABSTRACT

Numerous in-vitro studies have established that cells react to their physical environment and to applied mechanical loading. However, the mechanisms underlying such phenomena are poorly understood. Previous modelling of cell compression considered the cell as a passive homogenous material, requiring an artificial increase in the stiffness of spread cells to replicate experimentally measured forces. In this study, we implement a fully 3D active constitutive formulation that predicts the distribution, remodelling, and contractile behaviour of the cytoskeleton. Simulations reveal that polarised and axisymmetric spread cells contain stress fibres which form dominant bundles that are stretched during compression. These dominant fibres exert tension; causing an increase in computed compression forces compared to round cells. In contrast, fewer stress fibres are computed for round cells and a lower resistance to compression is predicted. The effect of different levels of cellular contractility associated with different cell phenotypes is also investigated. Highly contractile cells form more dominant circumferential stress fibres and hence provide greater resistance to compression. Computed predictions correlate strongly with published experimentally observed trends of compression resistance as a function of cellular contractility and offer an insight into the link between cell geometry, stress fibre distribution and contractility, and cell deformability. Importantly, it is possible to capture the behaviour of both round and spread cells using a given, unchanged set of material parameters for each cell type. Finally, it is demonstrated that stress distributions in the cell cytoplasm and nucleus computed using the active formulation differ significantly from those computed using passive material models.

Abbreviations: SF, stress fibre; RVE, representative volume element; E, Young's modulus; ν, Poisson's ratio; SMCs, smooth muscle cells; MSCs, mesenchymal stem cells; FBs, fibroblasts; *nuc*, nucleus; σ_{vm}, tensile equivalent stress, or, von Mises stress

*Corresponding author. Tel.: +1 353 91 493165; fax: +1 353 91 563991.
E-mail addresses: w.ronan1@nuigalway.ie (W. Ronan), vsd@eng.cam.ac.uk (V.S. Deshpande), rmcm@engineering.ucsb.edu (R.M. McMeeking), patrick.mcgarry@nuigalway.ie (J.P. McGarry).

1751-6161/$ - see front matter © 2012 Elsevier Ltd. All rights reserved.
http://dx.doi.org/10.1016/j.jmbbm.2012.05.016

1. Introduction

Previous in-vitro studies have established that cells react to their physical environment and to applied mechanical loading. Cells can sense and actively respond to the stiffness of an underlying substrate, with substrate stiffness affecting cytoskeletal remodelling (Byfield et al., 2009). Furthermore, it has been demonstrated that changes in cell shape or substrate stiffness can cause an increase in apparent cell stiffness (Janmey et al., 2011). However, the mechanisms underlying this active response of cells to the mechanical environment are poorly understood.

Cell compression has been used to quantify differences in the mechanical response of different cell types and shapes. Previous studies have used finite element models in tandem with experimentally measured geometries and compression forces to show that spread cells have a higher apparent stiffness than round cells for a range of different cell types (Caille et al., 2002; Darling et al., 2008). However, these models only consider the cell as a passive entity and assume either elastic, viscoelastic, or biphasic material behaviour. For such passive cell models, a given, unchanged set of material parameters cannot be used to replicate experimentally observed compression forces for round and spread cells. The apparent stiffness of spread cells must be artificially increased to account for the significant cytoskeletal remodelling that the cell undergoes as it changes from a round to a spread configuration (McGarry, 2009; McGarry and McHugh, 2008). In order to gain insight into the mechanisms underlying cellular cell stiffening, it is necessary to employ an active material model that predicts the distribution and contractility of the actin cytoskeleton.

The cytoskeleton has previously been modelled using pre-positioned passive filaments and contractility has been included as a prescribed thermal strain (Mohrdieck et al., 2005; Storm et al., 2005). However, these attempts have not considered the cellular processes that drive cytoskeletal remodelling and contractility. A recent study has proposed a novel computational model of contractile stress fibre (SF) behaviour based on the biochemistry of SF formation (Deshpande et al., 2007). This model is entirely predictive; i.e., the SF distributions and contractility are dynamically governed by cellular signalling and tension dependent dissociation. Models predicting SF formation and contractility have also been proposed by Kaunas and Hsu (2009), and Vernerey and Farsad (2011). All such models have been confined to 1D or 2D formulations; restricting SF formation to a single plane and restricting the ability to simulate in vitro experiments. The models of Kaunas et al. and Vernerey and Farsad differ from that of Deshpande et al. (2007): Vernerey and Farsad assume that the rate of SF formation is increased by fibre tension; Kaunas et al. assume that fibre dissociation occurs when a fibre has been stretched past a critical length. The Deshpande formulation has been used successfully to simulate SF distributions in cells on patterned substrates (Pathak et al., 2008). In a study by McGarry et al. (2009) this formulation is shown to accurately predict the scaling of active cell tractions with cellular contractility and with substrate stiffness for cells adhered to arrays of microposts.

In the current study, this formulation is expanded into a fully 3D framework that allows for the simulation of realistic round and spread cell geometries. This 3D implementation is used to investigate differences in SF evolution in a range of cell types with varying contractility. Simulations are performed for axisymmetric round and spread cells, and for a fully 3D elongated or polarised cell. The effect of cell shape and contractility on the compression response of cells is examined. The results of this study are compared to previous experimental data to illustrate the predictive capabilities of the model. Our findings highlight the importance of SF distribution and contractility in the mechanical response of a cell to applied compression.

2. Methods

2.1. Stress fibre contractility

Stress fibre (SF) formation consists of three coupled phenomena: an activation signal which triggers the formation of the SFs, dissociation of fibres due to a reduction in tension, and a Hill type law relating the contractility of a SF to strain rate.

The role of cellular signalling has been closely linked to cytoskeletal remodelling and mechanotransduction. In this study, the complete signalling pathway which triggers the SF formation is phenomenologically represented as an exponentially decaying signal (Roberts et al., 2001):

$$C = e^{(-t_1/\theta)} \tag{1}$$

where θ is a constant that controls the decay rate of the signal and t_1 is the time since the most recent signal.

Cytoskeletal tension is essential for sustaining SF bundles and a reduction below a defined isometric level leads to fibre dissociation (Franke et al., 1984; Kolega, 1986). The contractile behaviour of assembled SF bundles is similar to that of skeletal muscle. The tension in the SF bundle, which is generated by cross-bridge cycling of actin–myosin pairs (Warshaw et al., 1990), is related to the bundle contraction rate using the following Hill-like equation:

$$\frac{\sigma_f}{\sigma_0} = \begin{cases} 0 & \frac{\dot{\varepsilon}}{\dot{\varepsilon}_0} \le -\frac{\eta}{\bar{k}_v} \\ 1 + \frac{\bar{k}_v}{\eta}\frac{\dot{\varepsilon}}{\dot{\varepsilon}_0} & -\frac{\eta}{\bar{k}_v} \le \frac{\dot{\varepsilon}}{\dot{\varepsilon}_0} \le 0 \\ 1 & \frac{\dot{\varepsilon}}{\dot{\varepsilon}_0} > 0 \end{cases} \tag{2}$$

where σ_f is the stress in the SF bundle, σ_0 is the isometric tension, and $\bar{k}_v$ is the reduction in stress upon increasing the shortening strain rate $\dot{\varepsilon}$, by $\dot{\varepsilon}_0$. The dimensionless activation level of a SF bundle, η, at any orientation, also defines the isometric tension, σ_0, where $\sigma_0 = \eta\sigma_{max}$. σ_{max} is the maximum tension in a fully activated bundle. Fig. 1 shows the variation in tension with strain rate for each part of Eq. (2).

SFs are described by defining the dimensionless activation level η:$\eta(0 \le \eta \le 1)$, where $\eta = 1$ corresponds to the maximum possible SF activation level allowed by the biochemistry. The signal induced formation and tension dependent dissociation of the actin cytoskeleton is captured using a first order kinetic equation (Deshpande et al., 2007):

$$\dot{\eta} = [1-\eta]\frac{C\bar{k}_f}{\theta} - \left(1-\frac{\sigma_f}{\sigma_0}\right)\eta\frac{\bar{k}_b}{\theta} \tag{3}$$

the overdot denotes change with respect to time. The first term on the RHS governs the rate of formation of the SFs and is controlled by the dimensionless constant $\bar{k}_f$, the signal C, and decay constant θ. The latter part of the equation gives the rate of dissociation and is governed by the dimensionless constant $\bar{k}_b$, the stress level σ_f, and the isometric tension σ_0.

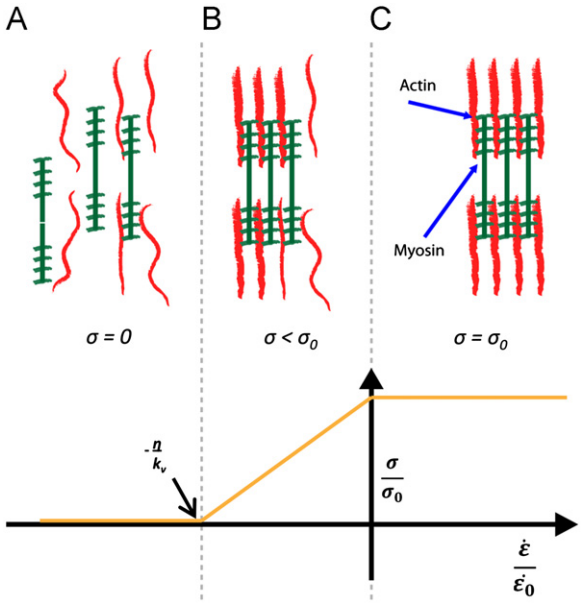

Fig. 1 – Actin–myosin stress fibre (SF) behaviour for each part of Eq. (2). A—Fibres with a large shortening rate have no tension and will dissociate quickly. B—Fibres with a shortening rate greater than $-\eta/k_v$ display a Hill like behaviour where tension is proportional to strain rate. C—Fibres with a positive strain rate are at isometric tension ($\sigma_0=\eta\sigma_{max}$) and do not dissociate.

2.2. Numerical implementation

In order to reduce computational cost, an axisymmetric cell geometry is assumed. However, as shown in Fig. 2, it is necessary to consider fibre orientations in 3D, as fibres are not confined to the radial plane. A representative volume element (RVE) is defined as a sphere with radius ρ containing SFs that are equally distributed in 3D space such that the distance between each fibre and its neighbour is minimised, as shown inset in Fig. 2. The orientation of an arbitrary fibre within the RVE is defined using the unit vector $\boldsymbol{m} = \sin(\omega)\cos(\varphi)\mathbf{x}_1 + \sin(\omega)\sin(\varphi)\mathbf{x}_2 + \cos(\omega)\mathbf{x}_3$. where $\mathbf{x}_i$ are the unit base vectors for a Cartesian basis in the current configuration. The strain rate $\dot{\varepsilon}_f$ in an arbitrary direction $\boldsymbol{m}$ can be determined from the strain state in the RVE using the following equation:

$$\begin{aligned}\dot{\varepsilon}_f = \dot{\varepsilon}_{ij}m_i m_j = {} & \dot{\varepsilon}_{11}\sin^2\omega\cos^2\phi + \dot{\varepsilon}_{22}\sin^2\omega\sin^2\phi + \dot{\varepsilon}_{33}\cos^2\omega \\ & +2\dot{\varepsilon}_{12}\cos\phi\sin\phi\sin^2\omega - 2\dot{\varepsilon}_{23}\sin\omega\cos\omega\sin\phi \\ & -2\dot{\varepsilon}_{13}\sin\omega\cos\omega\cos\phi\end{aligned} \tag{4}$$

The contribution of all fibres to the stress state in the RVE can be calculated by integrating over the volume:

$$\sigma_{ij} = \frac{1}{V}\int_V \sigma_f(\omega\varphi)m_i m_j dV \tag{5}$$

This integral can be approximated numerically by considering a finite number of fibres that extend from the centre of the RVE to equidistant points on the sphere surface. The stress tensor in the Cartesian basis generated by the active SF contractility is given as

$$\sigma_{ij}^{A} = \sum_{k=1}^{n}\frac{\sigma_f(\omega_k\phi_k)}{n}m(\omega_k\phi_k)_i m(\omega_k\phi_k)_j \tag{6}$$

where n is the number of fibre orientations. A sensitivity analysis of the number of fibre directions n revealed that convergence is achieved for $n=240$.

In parallel to the active SF behaviour described above, the passive material surrounding the SFs in the cell cytoplasm is modelled using a compressible neo-hookian hyperelastic

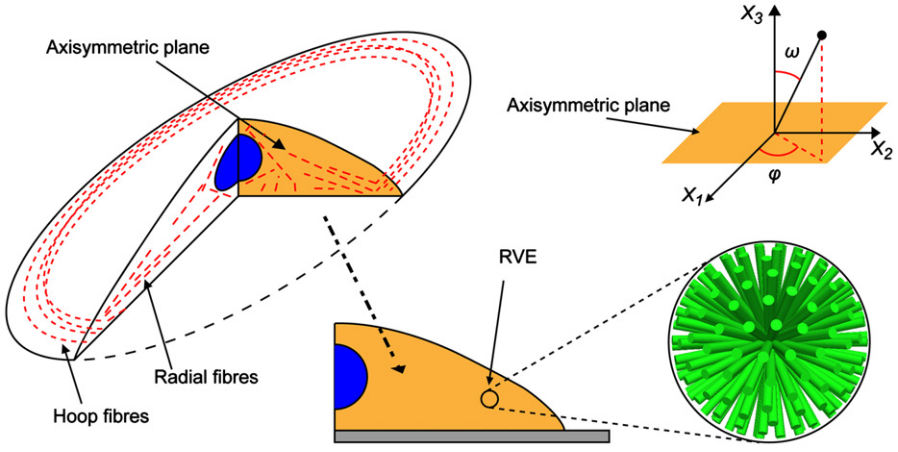

Fig. 2 – Schematic diagram of a 3D cell showing detail of the radial plane with circumferential (hoop) and radial SFs shown in red and the nucleus shown in blue. Inset shows 240 fibre orientations within the representative volume element. Unit vector m and angles (ω,ϕ) used to define its orientation are shown top right. (For interpretation of the references to color in this figure legend, the reader is referred to the web version of this article.)

formulation, whereby the passive stress tensor is given as

$$\sigma_{ij}^{P} = \frac{2}{J} C_{10}\left(\overline{B}_{ij} - \frac{1}{3}\overline{B}_{kk}\delta_{ij}\right) + \frac{2}{D_1}(J-1) \tag{7}$$

where the deviatoric left Cauchy–Green tensor $\overline{B}$ is determined from the deformation gradient F:

$$\overline{B}_{ij} = \frac{B_{ij}}{J^{2/3}} = \frac{F_{ik}F_{jk}}{(\epsilon_{lmn}F_{1l}F_{2m}F_{3n})^{2/3}} \tag{8}$$

The elasticity constants are given in terms of Young's modulus, E, and Poisson's ratio, ν, as:

$$C_{10} = \frac{E}{4(1+\nu)}, \quad D_1 = \frac{6(1-2\nu)}{E} \tag{9}$$

The complete stress state at any point in the cell cytoplasm is then given as

$$\sigma_{ij} = \sigma_{ij}^{A} + \sigma_{ij}^{P} \tag{10}$$

This active constitutive formulation is implemented as a *user defined material subroutine* in the commercial software Abaqus (Dassault Systemes, RI). The cell nucleus is modelled as a passive hyperelastic material using the same formulation given in Eq. (7). The subscript "$_{nuc}$" is used to denote material properties for the nucleus.

2.3. Finite element models

Finite element meshes of round and spread cells were generated based on previously reported cell geometries of such cells (Caille et al., 2002; Thoumine et al., 1999) as shown in Fig. 3. The initial dimensions of the cell used for each model are shown in Fig. 3. Axisymmetry is assumed for the round and spread cells shown in Fig. 3A and B. An elongated or polarised cell with an elliptical surface area is shown in Fig. 3C; however, it is sufficient to model one quarter of the polarised cell as it contains two symmetry planes. Thus a spread geometry is assumed for the cells in Fig. 3(A) and (C) prior to introduction of cellular contractility. The finite element model of each cell consists of two regions with different materials. The green regions in Fig. 3 represent the cytoplasm and material consists of the active formulation in parallel with a passive hyperelastic material as described above. The blue regions represent the nucleus and the material is simulated using a hyperelastic material. The two regions are continuous and no slip is permitted between the nucleus and cytoplasm. A nominal element size of 0.075 μm was chosen for all meshes. A mesh sensitivity study was performed and no changes to the results were observed for smaller element sizes. The cells are attached to a rigid substrate using a previously published cohesive zone model that captures the tension dependent formation of focal adhesions (Deshpande et al., 2008). An overview of this model is given in Appendix A. The cohesive zone model is implemented as a *user defined interface subroutine* in Abaqus.

In the first step of the simulation, fibre growth is driven by an exponentially decaying signal. The cell contracts on the rigid substrate due to the formation and remodelling of contractile SFs. Remodelling of the cytoskeleton continues until it reaches a steady state reached. Changes in cell height and nucleus shape also reach equilibrium during this step.

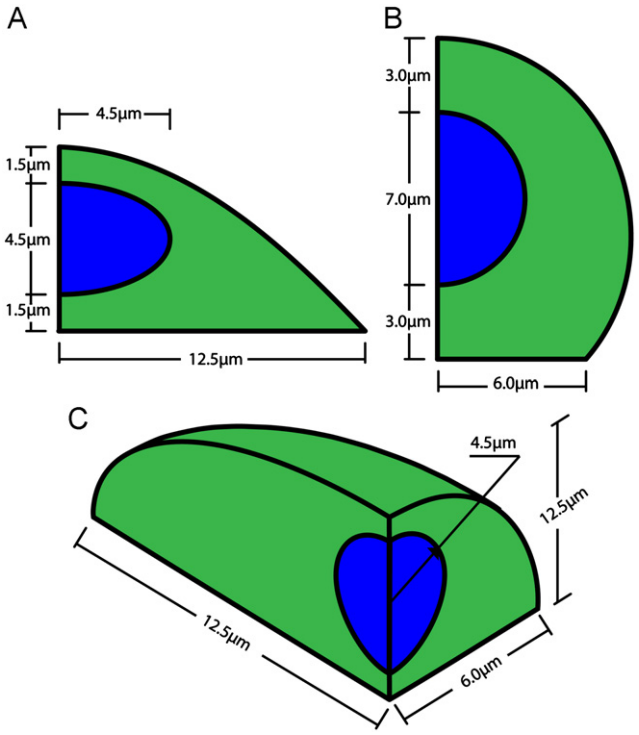

Fig. 3 – Dimensioned diagram of spread (A), round (B), and polarised (C) cell geometries. The nucleus is shown in blue and the cytoplasm is shown in green. Due to axial symmetry it is only necessary to consider the half cell plane shown here for (A) and (B). The polarised cell contains two vertical symmetry planes and the cell is simulated using the quarter cell geometry shown. (For interpretation of the references to color in this figure legend, the reader is referred to the web version of this article.)

Following from this, in the second step of the simulation, the cell is compressed to 30% of its steady state height, which was computed in step 1. A flat rigid indenter is brought into contact with the cell and moved downwards at a constant velocity of 0.02 μm/s. The effect of friction between the indenter and the cell was investigated for smooth frictionless contact, contact with different friction coefficients, and for rough contact. Friction was found to have a negligible effect (<1%), therefore hard, frictionless contact is used to describe the interaction between the cell and the rigid indenter.

2.4. Model parameters and interpretation of results

Different levels of contractility are investigated in this study in order to represent different cell phenotypes. Specifically, σ_{max} values of 25 kPa, 8 kPa, and 3.5 kPa are used to represent smooth muscle cells (SMCs), mesenchymal stem cells (MSCs), and fibroblasts (FBs) respectively, based on previous calibrations for 2D simulations of cells on microposts (McGarry et al., 2009). A passive cytoplasm stiffness of E_{cell}=0.4 kPa is chosen for all cell types, and completely passive cells are represented by bare cytoplasm (i.e. σ_{max}=0). For all cell types, the additional active parameters are set to θ=70s, k_v=7, $k_b = 1$, $\dot{\varepsilon} = 0.003\ s^{-1}$. Previous experimental studies of isolated

nuclei have estimated that the nucleus may be over 10 times stiffer than the cytoplasm (Thoumine et al., 1999). Therefore a passive nucleus stiffness of $E_{nuc}=4.0$ kPa is assumed.

In order to visualise the resulting 3D SF $E_{nuc}=4.0$ kPa $\bar{\eta}$ at each integration point, given as

$$\bar{\eta}=\sum_{k=1}^{n}\frac{\eta_k}{n} \tag{11}$$

where n is the total number (240) of discrete fibre orientations at each point. Secondly, in order to identify regions of the cell cytoplasm in which SFs are aligned in a dominant direction, a variance is defined to quantify the difference between the most highly activated fibre, η_{max}, and the average fibre activation, $\bar{\eta}$, at each integration point. The variance Π is defined as

$$\Pi=\eta_{max}-\bar{\eta} \tag{12}$$

Finally, vector plots are presented to illustrate the 3D orientation of dominant SFs throughout the cytoplasm.

3. Results

3.1. Stress fibre orientation and distribution

The distribution of the average SF activation level, $\bar{\eta}$, is presented in Fig. 4 for round and spread SMCs. In both cases, a steady state distribution has been achieved following signal driven SF evolution. For both the round and spread cell, SFs are seen around the nucleus and along the base, where the cell is attached to a rigid substrate. It is important to note that the spread cell shows significantly higher levels of SF formation than the round cell, with a distinctive band of SFs leading from the cell periphery over the top of the nucleus. In contrast, large areas of the round cell cytoplasm contain no SF formation and there are no bands extending from the nucleus to the cell periphery. The stiff nucleus and the attachment to the rigid substrate support tension in the SFs and, in accordance with Eqs. (2) and (3), these fibres do not dissociate. The spread cell, which has a significantly larger adhesion area, provides more support to the SFs, preventing fibres from dissociating. In the round cell there is a smaller adhesion area and the cell radius is larger than the adhesion radius. Consequently, there is not enough support for fibre tension, leading to shortening of fibres and fibre dissociation.

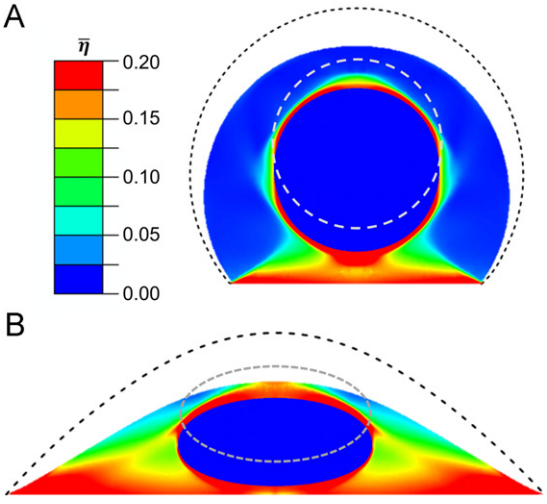

Fig. 4 – Average stress fibre (SF) level $\bar{\eta}$ for round (A) and spread (B) smooth muscle cells. Note the bands of SFs in the spread cell leading from the top of the nucleus to the cell periphery. In contrast, much of the round cell contains low levels of SFs. The dashed lines depict the original cell size prior to the introduction of cellular contractility.

In Fig. 5, vectors indicating the direction and activation level of the most highly activated SF at each integration point are plotted, with the results corresponding to the state of the SMCs in Fig. 4. The colour of the background and of the vectors corresponds to the variance (Π) at each integration point. Long, red fibres indicate that the SFs have formed dominant bundles in a particular direction. Blue areas with very short or no fibres have very low SF formation in all directions. Magnified views of the round cell in Fig. 5(C, D) reveal that dominant SF bundles around the nucleus are oriented in the radial plane. These fibres have formed in a narrow band all around the nucleus. SFs at the base of the round cell are oriented at approximately 45° to the radial plane (Fig. 5(E)). In contrast, Fig. 5(B, G, H) show that large areas of the spread cell contain dominant bundles of SFs that are oriented circumferentially.

The angle of a fibre to the radial plane ($\pi/2-\omega$) is shown in Fig. 6 (inset). The distribution of this angle for each integration point in SMCs corresponding to the condition depicted in Figs. 4 and 5 is presented in a histogram for both round and spread cells. For the spread cell, dominant fibres are oriented at 60°–90° to the radial plane, i.e., circumferential (hoop) fibres. In contrast, the dominant fibres in the round cell are mostly radial ones that form an angle of 0°–15° to the radial plane. Additionally, it should be noted that there is a higher level of fibre activation in the spread cell.

3.2. Cells under compression

Following the simulation of SF evolution to a steady state in response to an exponentially decaying signal, parallel plate compression of cells to 30% of the steady state cell height is then simulated. Compression forces are presented in Fig. 7 for round and spread SMCs. The round cell generates a peak force of ~350 nN at 70% compression strain (i.e. the cell height is 30% of the original value). However, significantly larger reaction forces are computed for the spread cell, with a peak force of ~1317 nN. As the cell is compressed, the dominant fibres identified in Fig. 5 undergo stretching. The majority of these dominant fibres are oriented in the circumferential direction and it should be noted that circumferential strain is higher at the cell periphery.

During compression of spread cells, these dominant contractile fibres are stretched and thus remain at a tension equal to the isometric level σ_0, providing resistance to cell compression. In these dominant fibres, the activation level is predicted to be close to its maximum value $\eta\approx1$, therefore the computed isometric tension level is equal to the maximum possible value $\sigma_0\approx\sigma_{max}$. In contrast, fibres in the round cell which are stretched during compression are found to

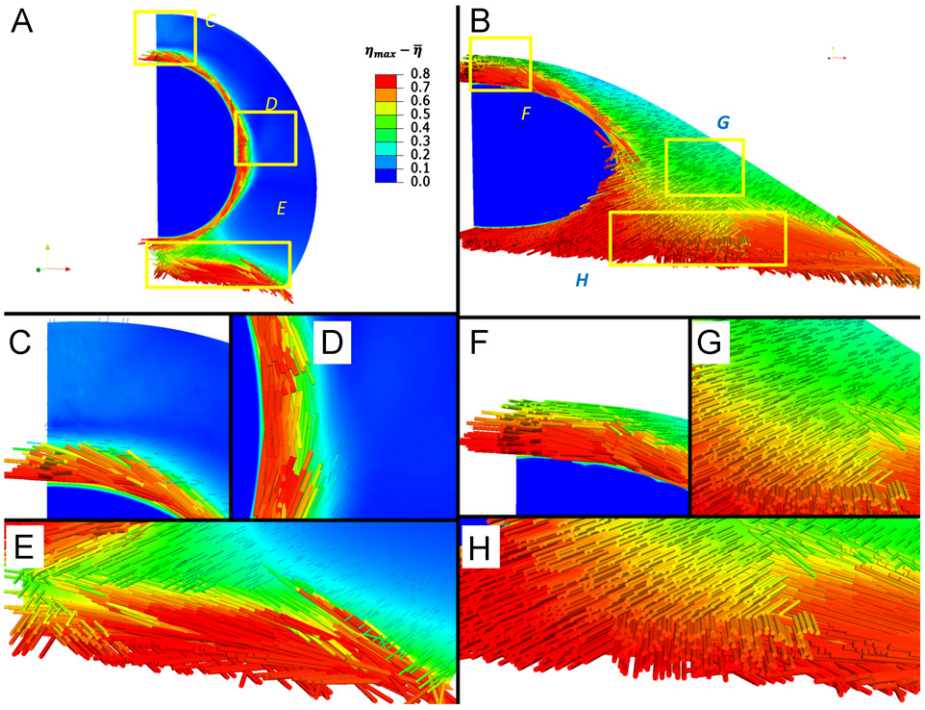

Fig. 5 – Orientation of the most highly activated fibre is shown for round (A) and spread (B) smooth muscle cells. Vector length and orientation describe the most highly activated fibre, where length is proportional to the activation level. The colour corresponds to the variance at each point. Long red fibres indicate that the stress fibres (SFs) have formed dominant bundles in a single orientation. Blue areas with short or no fibres have very low SF formation in all directions. Fibre orientation is shown in detail in for each cell: above the nucleus (C, F), in the cytoplasm (D, G), and at the base of the cell (E, H). (For interpretation of the references to color in this figure legend, the reader is referred to the web version of this article.)

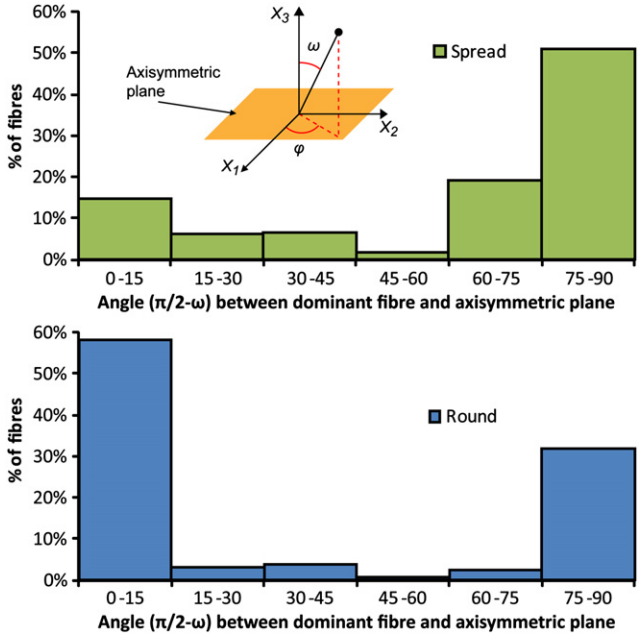

Fig. 6 – Distribution of angle ($\pi/2-\omega$) between radial plane and η_{max} orientation for all fibres for round (top) and spread (bottom) smooth muscle cells. An angle of 90 degrees means that fibres are in the hoop direction, and 0 degrees means the fibres are in the radial plane.

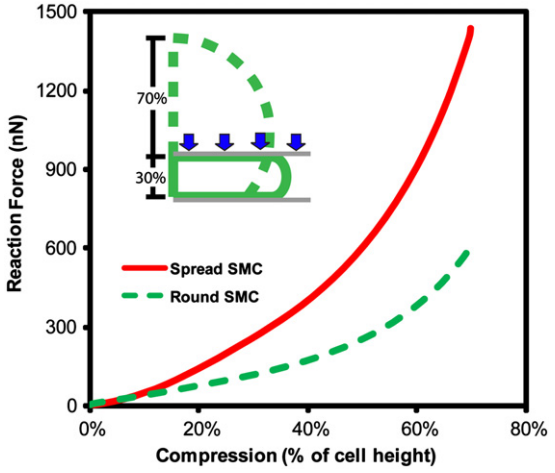

Fig. 7 – Compression reaction forces for round and spread smooth muscle cells when strained to as little as 30% of the original cell height. Note that the peak reaction force for the spread cell (1439 nN) is ~2.2 times larger than for the round cell (635 nN).

have a very low activation level $\eta \ll 1$. Furthermore, the majority of dominant fibres in the round cell do not undergo stretching during compression. The tension in these fibres

drops (as prescribed in Eq. (2)) and consequently, fibres are predicted to provide little resistance to compression.

3.3. *Effect of cellular contractility*

In addition to the previous simulations, where material properties were based on SMCs, the response of MSCs and FBs was also investigated by varying σ_{max} as outlined in Section 2.4. Fig. 8 shows the SF variance Π for cells following initial signal driven SF growth. FBs, which are the least contractile cells, have the lowest variance. The lower variance is due to a combination of higher average SF formation and a reduction in the activation level of the most highly activated fibre. The lower σ_{max} causes less contraction of the cell, which in turn leads to less fibre shortening in all directions and therefore less dissociation of SFs. Consequently, highly aligned contractile bundles do not readily form.

The peak reaction forces are shown in Fig. 9 for each cell type at 70% compression strain. Reaction forces for fully passive or non-contractile cells are also included for comparison. The peak force for both round and spread cells decreases with decreasing contractility. The peak force for the spread cell is reduced from 1736 nN for SMCs to 659 nN and 335 nN for MSCs and FBs respectively. This reduction is due to lower isometric tension in the dominant fibres in less contractile cells. The predicted isometric tension $\sigma_0=\eta\sigma_{max}$ is lower in contractile cells for two reasons: (i) the computed activation level η in the dominant direction is found to be lower, as shown in Fig. 8; (ii) the prescribed maximum fibre stress σ_{max} is lower (8 kPa and 3.5 kPa for MSCs and FBs, respectively). As is also evident in Fig. 9, the ratio of compression forces between spread and round cells increases with increasing cell contractility. A ratio of 2.9 is computed for SMCs compared to a ratio of 1.2 for passive non-contractile cells ($\sigma_{max}=0$). Therefore, changes in the cell geometry do not cause the stiffer response predicted for spread cells; the computed increase in force is due to the presence and orientation of dominant fibres which are stretched during compression of highly contractile spread cells.

3.4. *Stresses in cells*

Fig. 10 shows the tensile equivalent stress (also known as the von Mises stress) in axisymmetric cells before and after compression. The cytoplasm stress tensor is defined according to Eq. (10) and the tensile equivalent stress is defined by

$$\sigma_{vm}=\sqrt{\frac{3}{2}S_{ij}S_{ij}};\quad S_{ij}=\sigma_{ij}-\frac{\sigma_{kk}}{3}\delta_{ij} \tag{13}$$

Compression of round and spread SMCs causes a ~2 fold increase in stress throughout the cytoplasm and more than a ~10 fold increase in the nucleus (Fig. 10(A–D)). In the spread FB, the stress in the cytoplasm before compression is ~5 times lower than the spread SMC. Fig. 10(G) shows that the stress in the nucleus is significantly lower in FBs than in SMCs (Fig. 10(C)) before compression. After compression, FB cytoplasm stress increase by a factor of ~2 (Fig. 10(F)). However, nucleus stresses increase by a factor of ~30. Finally, Fig. 10(H) shows the stress distribution in passive cells following compression. Stresses are highly localised above and below the nucleus. This distribution differs significantly from the predicted stress distributions for SMCs (Fig. 10(B, D)).

3.5. *Stress fibre formation in polarised cells*

Fig. 11 shows SF orientation and distribution in a polarised SMC after SF formation has reached steady state in response to an exponentially decaying signal. A quarter cell showing fibre orientations on 3 orthogonal planes is shown in Fig. 11(A), i.e., the two vertical planes of symmetry and a

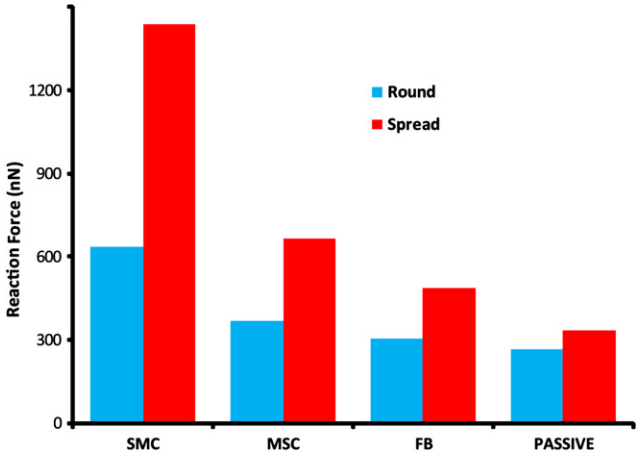

Fig. 9 – Peak reaction forces at 70% compression strain for round and spread cells. The peak force ratio for spread to round is 2.3, 1.8, 1.6, and 1.25 for smooth muscle cells (SMCs), mesenchymal stem cells (MSCs), fibroblasts (FBs) and passive cells respectively.

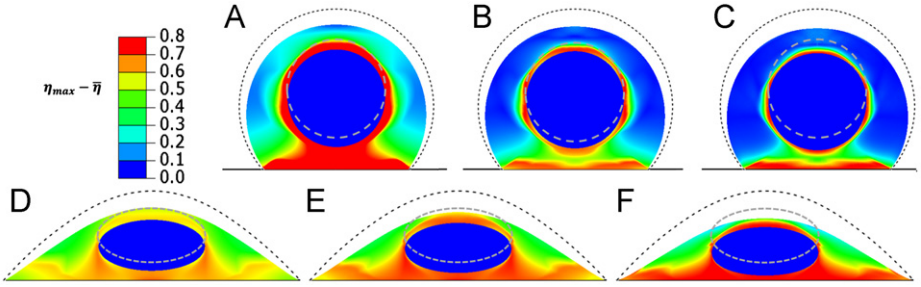

Fig. 8 – Stress fibre variance [Π] for round (top) and spread (bottom) cells for fibroblasts (FBs) (A, D), mesenchymal stem cells (B, E), and smooth muscle cells (C, F). Note that the variance is lowest for the FBs, which are the least contractile cells. The dashed lines depict the original cell geometry prior to the introduction of cellular contractility.

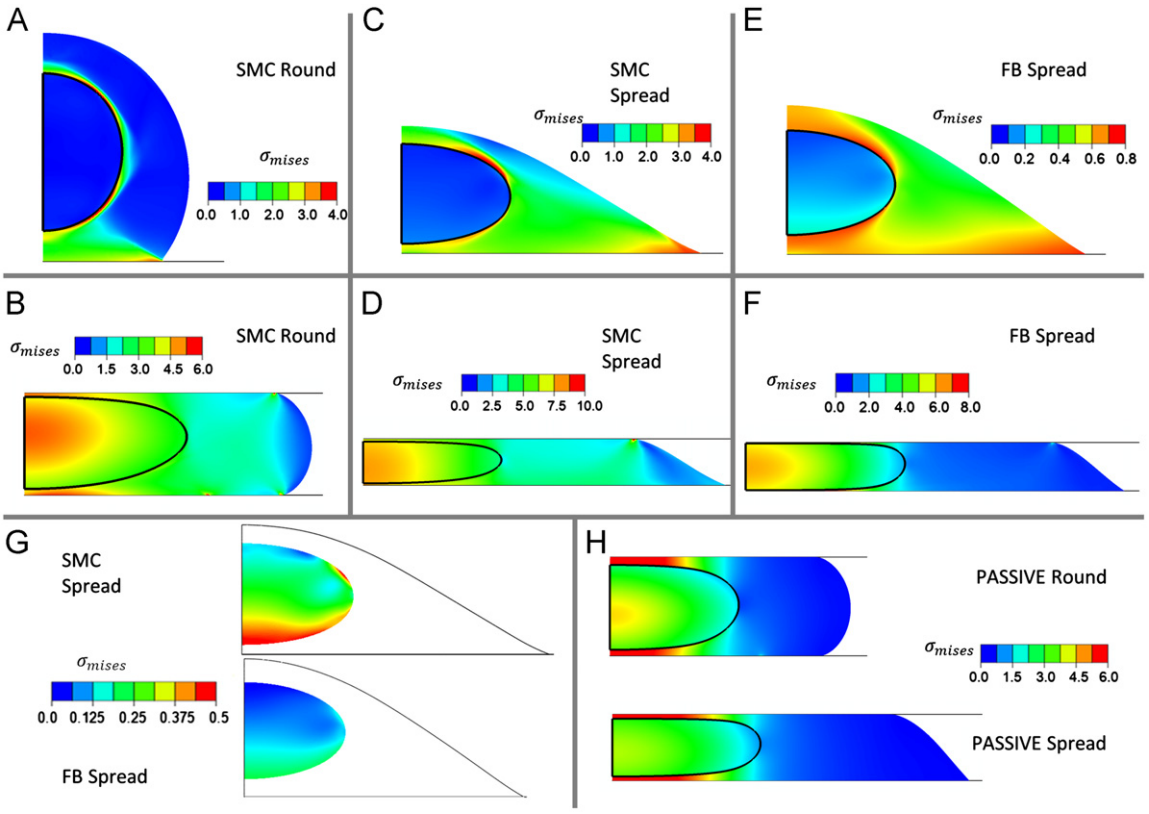

Fig. 10 – Tensile equivelent stress (also known as the von Mises stress) before and after compression for round smooth muscle cells (SMCs) (A, B), spread SMCs (C, D), and spread fibroblasts (FBs) (E, F). Von Mises stress is shown for the nucleus only for SMCs and FBs before compression (G). Stresses are also shown for passive cells after compression.

horizontal plane at the cell base. SFs are further illustrated in the horizontal basal plane in Fig. 11(B) and in additional vertical planes in Fig. 11(C). In order to further visualise the 3D SF distribution throughout the entire cytoplasm a 3D animation is presented in two videos in the online supplementary material (Movie S1, S2). Dominant fibre bundles are predicted to form parallel to the long axis of the cell. Due to the polarised shape of the cell, the cell is more deformable in the direction of the minor axis, which leads to fibre shortening and dissociation in this direction. In contrast, the cell is less deformable in the direction of the major axis, supporting fibre tension and preventing dissociation. Similar to axisymmetric cells, SF activation levels are highest at the base of the cell near the adhesion to the rigid substrate where fibre tension is supported, preventing fibres from dissociating.

Supplementary material related to this article can be found online at http://dx.doi.org/10.1016/j.jmbbm.2012.05.016.

3.6. *Compression and release of polarised cells*

As implemented for axisymmetric cells, polarised cells were compressed to 30% of the steady state height following the signal driven growth described above. The simulated compression forces are presented in Fig. 12(A) for SMCs, MSCs, FBs, and a passive cell with no contractility. Similar to axisymmetric cells, larger compression forces predicted for highly contractile cells; a peak reaction force (after compression to 30%) of 2340 nN is computed for SMCs, 1270 nN for MSCs, 945 nN for FBs, and 700 nN for passive cells. The increased compression resistance computed for highly contractile polarised cells is due to the stretching of dominant SF bundles. Fig. 12(C) shows dominant fibre bundles that are stretched during compression for a cell that has been compressed to 50% of its steady state height, i.e., dominant fibres that are not undergoing stretch are not shown. These SFs have a high activation level and have a positive strain rate; therefore they exert an isometric tension close to the maximum possible value in accordance with Eq. (2), $\sigma_0 = \eta\sigma_{max} \approx \sigma_{max}$. Although the prediction of long parallel SFs for polarised cells differs from the circumferential SFs computed for axisymmetric cells, the dominant fibre bundles in both geometries are stretched during compression, and SF tension causes an increase in compression resistance. Compression and release of a polarised cell is shown in an animation in the online supplementary material (Movie S3). Increasing the Poisson's ratio of the cell from 0.3 to 0.4 resulted in an ~18% increase in compression reaction forces for both passive and active cells (data not shown).

Following compression to 30% of the steady state height, the indenter is immediately withdrawn and the cell is allowed to return to an equilibrium configuration. The recovery of the cell height is shown in Fig. 12(B) for each contractile cell type. In the 1200s following the release both the MSC and FB recover to a steady state value, with the least contractile FB recovering fastest. As the cell relaxes, fibres which were stretched during compression are now shortening. The tension in these

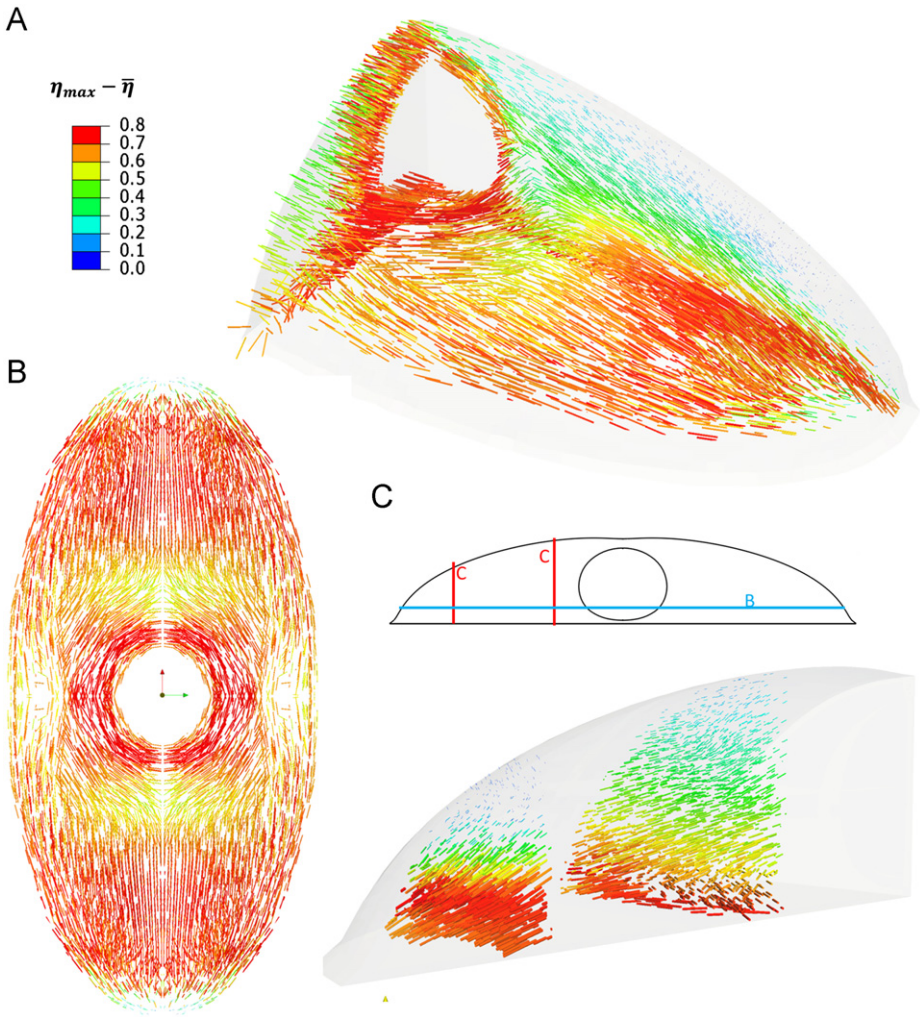

Fig. 11 – Stress fibre (SF) orientation is shown for an smooth muscle cells (SMC) with a polarised cell geometry. Vector length and orientation describe the most highly activated fibre, where length is proportional to the activation level and the colour corresponds to the variance at each point. SFs are plotted on 3 orthogonal planes (A), with 2 vertical symmetry planes and a horizontal plane near the base of the cell. SFs are further illustrated on the horizontal plane (B) and on two additional vertical planes (C). *Note:* SF distribution is computed throughout the cytoplasm and is further illustrated in Movie S1 in the online supplementary material.

shortening fibres drops, which leads to fibre dissociation. The time-dependent response computed for contractile cells in Fig. 12(B) is entirely due to SF dynamics described in Eqs. (2) and (3), as no viscoelasticity has been included in the material formulation. It should be noted that all cells have recovered to a cell height greater than the steady state value prior to compression. Although the SMC has not yet reached a steady state by 1200 s, it has relaxed to a height greater than that prior to compression. The steady state heights of MSCs and FBs have increased by 20% and 30%. SF dissociation during release leads to an overall drop in tension throughout the cell and consequently to an increase in the steady state height.

4. Discussion

The simulations presented here demonstrate that a computational model based on the active remodelling and contractility of stress fibres (SFs) captures the compression response of adherent cells. By implementing this predictive bio-chemo-mechanical formulation (Deshpande et al., 2007) in a fully 3D framework, it is shown that the orientation of dominant fibre bundles significantly influences the mechanical response of cells to compression. Specifically, if the dominant fibre bundles in the cell are stretched during compression, they significantly increase the computed compression force. In round cells, low SF formation is computed, with fibres occurring predominantly in the radial plane; hence, these fibres shorten during compression and therefore provide little resistance to compression. In contrast, high SF formation is computed for both axisymmetric and polarised spread cell geometries and, generally, the dominant fibres are stretched during compression. The resultant isometric fibre tension causes a significant increase in compression resistance. Simulated SF formation is significantly affected by cell shape, by the contractility level of the cell phenotype, and the

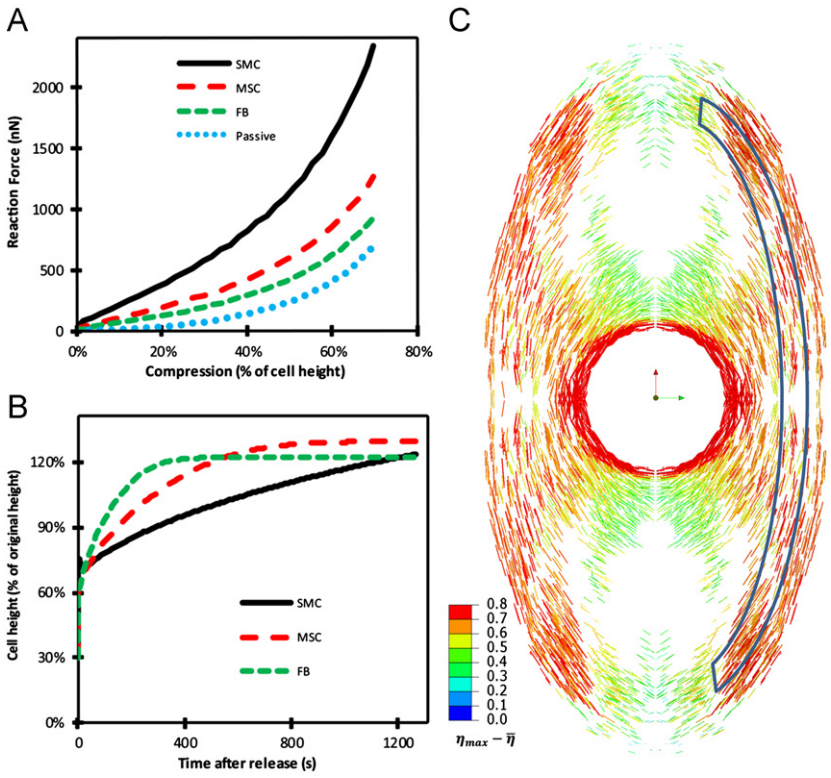

Fig. 12 – Compression reaction forces for smooth muscle cells (SMC), mesenchymal stem cells (MSC), fibroblasts (FB), and a passive cell with no stress fibres for cell compressed by 70% of their steady state height (A). Creep recovery curves for SMCs, MSCs and FBs following release after compression (B). Cell height was 30% of the original steady state height before release. Vector plot of dominant stress fibre bundles that undergo stretch during compression (C), i.e. dominant SF bundles that shorten during compression are not shown. The highlighted region represents a SF bundle running the length of the cell. These fibres remain at isometric tension, providing resistance to compression.

presence of the nucleus. In axisymmetric spread cells the dominant fibres are predicted to align in the circumferential direction and in polarised cells they are predicted to align parallel to the long axis of the cell. In comparison to SMCs, decreased levels of cellular contractility associated with MSCs and FBs alter SF distributions and cause a reduction in the computed reaction forces. SF distributions and compression forces for both round and spread cells are simulated using a given, unchanged set of material parameters for each of three cell phenotypes.

In the present study, SF distributions and compression forces for both round and spread cells are simulated using a given, unchanged set of material parameters for each of three cell phenotypes. Simulations predict that spread cells have significantly more dominant SF bundles than round cells. In axisymmetric spread cells, these are oriented in the circumferential direction and in polarised cells these are parallel to the major cell axis. In both axisymmetric and polarised spread cells, our model is in strong agreement with experimentally observed distributions. The following experimental observations are reported for cells displaying an approximately axisymmetric geometry: Potter et al. (1998) show axisymmetric fibroblasts with clearly defined actin SFs oriented circumferentially near the cell periphery; Goffin et al. (2006) show that myofibroblasts on micropatterned substrates and on istropic substrates fibroblasts acquire an axisymmetric shape with actin SFs throughout the cytoplasm; Schober et al. (2007) also show distinct bands of circumferential fibres for keratinocytes. Cells with polarised geometries are reported to have long parallel fibres: Peeters et al. (2004) show elongated myoblasts with distinctive long SFs parallel to the long edge of the cell; Goffin et al. (2006) also show elongated myofibroblasts with long parallel fibres oriented with the long axis of the cell; finally Engler et al. (2006) show polarised cells with long parallel fibres for MSCs seeded on glass substrates. In contrast, experimental images of rounded cells, such as unspread chondrocytes, show no distinct alignment of fibres, with actin staining having a smeared appearance throughout the cytoplasm (Ofek et al., 2009a). This is captured by our simulations of round cells, where low SF activation levels are predicted $\bar{\eta}(\ll 1)$, with no dominant bundling direction $\Pi(\ll 1)$ in most of the cytoplasm. The present study also demonstrates that the nucleus plays a significant role in SF formation by providing a stiff structure around which a thin band of SFs form. As a stiff structure in the centre of the cell, the nucleus provides support for the tension that is essential for the persistence of SFs. Houben et al. (2007) give a comprehensive review of the importance of structural interactions between the nucleus and the cytoskeleton. Broers et al. (2004) also report a significant decrease in compression resistance for cells in which nuclear lamins have been removed. Broers et al. further show that the

removal of nuclear lamins also causes disruption of the actin cytoskeleton and a decrease in cell stiffness. Khatau et al. (2009) also highlight the structural relationship between the nucleus and the actin cytoskeleton in spread cells.

Circumferential SFs have been described by Naumanen et al. (2008) as transverse arcs. Such transverse arcs are generated from α-actinin-decorated actin filaments which assemble endwise with myosin bundles to form contractile transverse arcs. The contractile nature of these transverse arcs is confirmed by Hotulainen and Lappalainen (2006) where myosin ATPase activity is inhibited by treating cells with blebbistatin. This cell treatment resulted in complete dissociation of transverse arcs in the cell, and after 30 min focal adhesions disappeared. Furthermore, Oakes et al. (2012) report that transverse arcs generate large amounts of tension that is relayed to focal adhesions.

The current study predicts a stiffer response for spread cells compared to round cells. This result is supported by the experimental data of Darling et al. (2008) which reports significant differences in apparent cell stiffness between round and spread osteocytes (7.5 fold increase) and MSCs (4.5 fold increase). The experimental findings of Caille et al. (2002) suggest that the force required to compress endothelial cells is six times higher for spread cells compared to round cells. Previous finite element simulations of cell compression have used passive material models, requiring an artificial increase in the passive stiffness of the cell material in order to capture the increased compression forces for spread cells (Caille et al., 2002; Thoumine et al., 1999). It is important to note that the active framework implemented in this study captures this trend while using a given, unchanged set of model parameters for each cell phenotype. The increased resistance of spread cells to compression results from the stretching of dominant contractile SF bundles. This mechanism is supported by the experimental observations of Peeters et al. (2004) for polarised cell geometries, where it is reported that long actin fibres restrict deformation of the cell and nucleus in the direction perpendicular to the dominant fibre orientation. This observation underlines the fully predictive nature of our modelling framework which provides an insightful link between cell geometry, SF distribution and response to mechanical stimuli. In the current study, for both axisymmetric and polarised spread cells, we predict a similar mechanism of increased compression resistance. In both cases the dominant fibre directions are oriented such that cell compression results in stretching of these fibres at isometric tension, leading to an increase in resistance to compression. In the case of axisymmetric cells, these dominant fibres occur in a circumferential direction whereas in a polarised cell these dominant fibres occur along the length of the cell.

The link between cell contractility and resistance to compression is further underlined by our prediction that increased cell contractility leads to an increase in compression force. In spread cells, the dominant fibre bundle is stretched during compression and these bundles exhibit tension equal to the isometric level $\sigma_0=\eta\sigma_{max}$. Therefore, higher levels of cellular contractility σ_{max}, which are associated with different cell phenotypes, result in higher tension in the dominant bundles and consequently a greater resistance to compression. The active modelling framework predicts that spread SMCs provide most resistance to compression (1400 nN), followed by MSCs (600 nN) and fibroblasts (400 nN). These predictions are strongly supported by previous experimental studies: peak reaction forces of 2500 nN have been reported for compression of highly spread myoblasts (Peeters et al., 2005). However, less contractile cells such as endothelial cells generate peak forces in the region of 500 nN (Caille et al., 2002) and spread fibroblasts generate a reaction force of ~360 nN (Lulevich et al., 2006). Lower forces have been observed experimentally for round cells, with ~100 nN being measured for round endothelial cells and ~80 nN for round chondrocytes (Ofek et al., 2009b). Furthermore, in the study of Darling et al. (2008), spread osteoblasts and MSCs were shown to be 4.5 and 2.3 times stiffer than spread chondrocytes, respectively. In contrast, round osteoblasts and MSCs were shown to be only 1.3 and 1.15 times stiffer than round chondrocytes.

The present study also suggests a link between contractility and creep recovery of a cell following compression. Upon removal of the indenter, the current study predicts a time-dependent recovery of the cell geometry to a steady state. The apparent relaxation time for FBs is similar to that reported by Thoumine and Ott (1997). Similarly shaped creep recovery curves have been reported by Ofek et al. (2009c) for chondrocytes, with a lower relaxation time of ~5 s, suggesting a faster recovery time for less contractile phenotypes. Our simulations suggest that this characteristic time-dependent response is primarily due to the remodelling and shortening of the dominant SF bundles as SFs are observed to dissociate both fibres when the cell is released (the converse of the lengthening of these fibres during the compression phase and the recovery phase). As fibres shorten, they obey a Hill-type tension-strain rate behaviour, with the fibre tension reducing from the isometric value. This tension reduction during release leads to partial fibre dissociation, further adding to the time dependent release behaviour. It is important to note that in the current study, unlike previous studies using simple standard viscoelastic material behaviour (Sato et al., 2006; Thoumine and Ott, 1997), no phenomenological viscoelasticity was used to capture this time-dependent behaviour, suggesting that SF dynamics contribute to the creep recovery of cells. This highlights the capability of our model to provide mechanistic insight in addition to quantitative prediction.

The mechanical cellular environment is closely linked to cell differentiation (Engler et al., 2006) and, in particular, the cytoskeleton provides a mechanical link from the nucleus to the extracellular matrix (Buxboim et al., 2010). Nucleus stresses play an important role in stem cell differentiation and significant differences have been reported between stem cells and differentiated cells in terms of nucleus stiffness and nucleus stresses (Pajerowski et al., 2007). The accurate prediction of cell and nucleus stresses would represent a significant step in understanding and controlling cell mechanotransduction. In the current study, we demonstrate that the stress distribution following compression in the cell and nucleus computed using a passive hyperelastic cytoplasm differs significantly to that computed using the active SF formulation. The passive formulation predicts highly

localised stress concentrations at the centre of the cell and very little stress in the peripheral regions of the cytoplasm, in contrast to the active formulations, where significant stresses are computed throughout the cytoplasm for highly contractile cells. In the experimental study of Pajerowski et al. (2007), the differences in nuclues stiffness between stem cells and differentiated cell were determined using the micropipette technique in tandem with a simple passive analytical solution for the deformation of the aspirated cell. Therefore the change in apparent stiffness of the nuclei during aspiration may be due to the increased contractility of differentiated cells, rather than a change in the stiffness of the nuclues material. Furthermore, the active formulation offers a prediction of cell and nucleus stresses in the absence of external stimuli.

In line with previous implementations of the material formulation (McGarry et al., 2009; Pathak et al., 2008) and experimental observations of chondrocytes and endothelial cells (Ferko et al., 2007; Shieh et al., 2006), a Poisson's ratio of 0.3 is assumed for the majority of simulations in the current study. Other experimental studies have observed a Poisson's ration of 0.4 (Freeman et al., 1994; Jones et al., 1999; Trickey et al., 2006); however, Darling et al. (2008) found that varying the Poisson's ratio between 0.3 and 0.5 only caused a $\pm$20% change in the apparent elastic modulus of the cell. In the current study, increasing the Poisson's ratio from 0.3 to 0.4 results in an $\sim$18% increase in compression reaction forces for both passive and contractile cells; suggesting that the ratio of active to passive compression force is independent of the Poisson's ratio. A previous investigation of the role of compressibility and Poisson's ratio for passive cells (McGarry, 2009) determined that assuming a fully incompressible cell (v=0.5) leads to significant bulging of the cell during compression. Such bulging is not consistent with the experimental images of compressed endothelial cells reported by Caille et al. (2002).

The model geometries in the current study are based on previous experimental observations of round and spread cells (Caille et al., 2002; Thoumine et al., 1999). However, these studies only investigated the mechanical response of actively contractile cells and did not isolate the role of the cytoskeleton through the use of SF inhibitors. The different levels of contractility associated with each cell type cause a reduction in cell height to a steady state value that is different for each cell type simulated. In order to overcome this limitation, all compression forces are presented as a function of change in cell height normalised by the steady state height. In a follow on experimental study, the effect of contractility on cell and nucleus height, presenting a framework to accurately parse the nucleus stiffness, cell contractility, and passive cytoplasm stiffnes in spread cells (Weafer et al., submitted for publication). Additionally, all cell types were simulated in the current study using the same passive material properties. Previous investigations have calculated stiffness values by assuming the cytoplasm and cytoskeleton form a passive homogenous material. In contrast, the passive stiffness used in the current study is separated from the active contribution of the SFs. In the current study, non-contractile elements such as microtubules and intermediate filaments have been represented using a non-linear hyperelastic continuum. However, previous experimental studies have shown that microtubules undergo more complex deformation; for example, Brangwynne et al. (2006) show that in unloaded cells the microtubule network can buckle under cellular contractility. A follow on experimental study will examine the role of both actin SFs and microtubules in the shear response of cells.

In the current study, each phenotype has been modelled by changing the cellular contractility, based on the calibration of cells on arrays of microposts and on patterned substrates (McGarry et al., 2009; Pathak et al., 2008). These previous implementations of the active SF formulation have been limited to 2D simplifications. In the current study, this framework has been extended so that SF evolution is predicted in a fully 3D environment. The alignment of dominant SF bundles which cause the increased resistance to compression in spread cells are not considered in a 2D formulation. Therefore, in order to accurately simulate experiments in which the cell deformation occurs in more than one plane, it is essential to consider SF formation in all directions. A 3D formulation also allows for the simulation of realistic polarised cell geometries and the inclusion of a cell nucleus. Cell compression has been used in a range of in vitro studies to quantify the mechanical properties of different cell types, including endothelial cells (Caille et al., 2002), fibroblasts (Thoumine and Ott, 1997, JCS), myoblasts, (Peeters et al., 2005), adipocytes (Or-Tzadikario and Gefen, 2011) and MSCs, osteoblasts, chondrocytes, adipocytes (Darling et al., 2008). Previous computational investigations have assumed axisymmetric geometries for compression (Caille et al., 2002; Nguyen et al., 2010; Ofek et al., 2009b) and micropipette aspiration (Haider and Guilak, 2002; Rowat et al., 2005) without investigating the effect of polarised cell geometries. The implementation of a fully 3D framework provides insight into the link between the contractility and alignment of dominant SFs and cellular resistance to compression. It should also be noted that the model parameters calibrated for the pseudo-2D environments of cells attached to micro-posts (McGarry et al., 2009) and cells on fibronectin patches (Pathak et al., 2008) are shown to provide reasonable predictions of compression forces compared to published experimental values. This illustrates the robustness and applicability of the active SF formulation to a wide range of single cell experiments.

In the current study, the contractile cytoskeleton has been considered in a 3D, predictive framework with no predefined SF arrangement. This implementation elucidates the role of the cytoskeleton in the response of different cell types and shapes to compression between two rigid plates. The orientation and distribution of fibres significantly affects the forces generated by the cells. In both axisymmetric and polarised cell geometries dominant bundles of highly aligned SFs are computed: in the case of axisymmetric cells such dominant bundles occur in the circumferential direction whereas for polarised cells dominant bundles occur parallel to the long axis of the cell. In both cases the dominant SF bundles are stretched at isometric tension during the compression event, leading to an increased resistance to cell compression. This effect is most pronounced for highly contractile cells. In contrast, round cells provide a low resistance to compression as lower levels of SF formation are predicted, and SF tension does not significantly contribute to compression resistance.

The framework presented here provides a powerful platform to consider the role of the cytoskeleton in different loading modes. In a follow-on study, this 3D framework will be used to investigate the mutual dependence of SF formation and focal adhesion assembly during cell spreading and for cells in 3D loading environments.

Acknowledgments

Funding support was provided by the Irish Research Council for Science, Engineering and Technology (IRCSET) postgraduate scholarship under the EMBARK initiative, and by the Science Foundation Ireland Research Frontiers Programme (08/RFP/ENM1726). The authors wish to acknowledge the SFI/HEA Irish Centre for High-End Computing (ICHEC) for the provision of computational facilities and support.

Appendix A1. Cohesive zone model

The adhesion of cells to a substrate is simulated using a recent thermodynamically motivated model (Deshpande et al., 2008). This model considers the formation of focal adhesions via the bonding of integrins on the cell surface to suitable ligands on the ECM. A brief overview is provided here; however, the reader is referred to the original publication for a detailed motivation and discussion.

A.1.1. *Thermodynamics of bond formation*

Binding integrins on the cell surface exist in two conformational states: high affinity, or "straight", integrins with a high reference chemical potential, χ_H , and low affinity, or "bent", integrins with lower reference chemical potential χ_L. Only the high affinity integrins form bonds and low affinity integrins remain unbound. Low affinity integrins with a concentration ξ_L have a chemical potential:

$$\chi_L = \mu_L + kT\ln\left(\frac{\xi_L}{\xi_0}\right) \tag{A.1}$$

where μ_L is the internal energy and the last term accounts for the configurational entropy. ξ_0 is the total concentration of integrins, and k and T are the Boltzmann constant and the absolute temperature.

High affinity integrins form bonds and undergo stretching, therefore the potential energy stored in the bond and the mechanical work done are accounted for in the chemical potential as

$$\chi_H = \mu_H + kT\ln\left(\frac{\xi_H}{\xi_0}\right) + \Phi(\Delta_i) - F_i\Delta_i \tag{A.2}$$

where Φ is the stretch energy and $F_i\Delta_i$ is the mechanical work due to the stretch Δ_i of the bond by the force F_i. The force F_i is related to the stretch by

$$F_i = \frac{\partial\Phi}{\partial\Delta_i} \tag{A.3}$$

The kinetics of bond formation and diffusion of low affinity integrins along the cell membrane are considered fast compared with other time scales involved. Therefore diffusive fluxes are neglected and the concentrations of the integrins are given by thermodynamic equilibrium: $\chi_H = \chi_L$. Therefore the concentrations of high and low affinity integrins are determined as

$$\xi_H = \frac{\xi_0}{\exp((\mu_H - \mu_L + \Phi - F_i\Delta_i)/(kT)) + 1} \tag{A.4a}$$

$$\xi_L = \frac{\xi_0}{\exp(-(\mu_H - \mu_L + \Phi - F_i\Delta_i)/(kT)) + 1} \tag{A.4b}$$

The stretch energy phi is expressed as a piecewise quadratic potential:

$$\Phi = \begin{cases} \kappa_s\Delta_e^2 & \Delta_e \le \Delta_n \\ -\kappa_s\Delta_n^2 + 2\kappa_s\Delta_n\Delta_e - (\kappa_s\Delta_e^2 & \Delta_n < \Delta_e \le 2\Delta_n \\ \kappa_s\Delta_n^2 & \Delta_e > 2\Delta_n \end{cases} \tag{A.5}$$

where κ_s is the stiffness of the bond; Δ_e is the effective stretch and Δ_n is the peak bond length. The bond stretch Δ_i is related to the displacement of the membrane relative to the ECM as

$$\Delta_i = \begin{cases} u_i & \Delta_e \le \Delta_n \text{ or } \left[\frac{\partial\Phi}{\partial\Delta_e}\Delta_e < 0\right] \\ 0 & \text{otherwise} \end{cases}. \tag{A.6}$$

A.1.2. *Finite element implementation*

The tractions on the cell surface depend on the force F_i on each bond and the concentration of bound high affinity integrins ξ_H such that:

$$T_i = -\xi_H F_i \tag{A.7}$$

These tractions are balance by stresses in the cell caused by cellular contractility such that:

$$T_i = \sigma_{ij}n_j = -\xi_H F_i \tag{A.8}$$

where σ_{ij} is the Cauchy stress in the cell, and n_j is the surface normal. In the current study, detachment of the cell from the substrate is not considered. Therefore the cell is constrained so that points that are in contact on the cell surface remain in contact, i.e. only tangential displacements are allowed.

The focal adhesion parameters are chosen based on previous calibrations of this model (Deshpande et al., 2008; Pathak et al., 2008) as: $(\mu_H - \mu_L) = 2.14 \times 10^{-20}$ J; $\xi_0 = 5000\ \mu m^{-2}$; $\kappa_s = 0.015$ nN μm^{-1}; $\Delta_n = 0.013\ \mu m$. A rigorous investigation of the interdependence of focal adhesions and cellular contractility will be presented in a follow up paper.

REFERENCES

Brangwynne, C.P., MacKintosh, F.C., Kumar, S., Geisse, N.A., Talbot, J., Mahadevan, L., Parker, K.K., Ingber, D.E., Weitz, D.A., 2006. Microtubules can bear enhanced compressive loads in living cells because of lateral reinforcement. The Journal of Cell Biology 173, 733–741.

Broers, J.L.V., Peeters, E.A.G., Kuijpers, H.J.H., Endert, J., Bouten, C.V.C., Oomens, C.W.J., Baaijens, F.P.T., Ramaekers, F.C.S., 2004. Decreased mechanical stiffness in LMNA−/− cells is caused by defective nucleo-cytoskeletal integrity: implications for the development of laminopathies. Human Molecular Genetics 13, 2567–2580.

Buxboim, A., Ivanovska, I.L., Discher, D.E., 2010. Matrix elasticity, cytoskeletal forces and physics of the nucleus: how deeply do cells 'feel' outside and in? Journal of Cell Science 123, 297–308.

Byfield, F.J., Reen, R.K., Shentu, T.P., Levitan, I., Gooch, K.J., 2009. Endothelial actin and cell stiffness is modulated by substrate stiffness in 2D and 3D. Journal of Biomechanics 42, 1114–1119.

Caille, N., Thoumine, O., Tardy, Y., Meister, J.-J., 2002. Contribution of the nucleus to the mechanical properties of endothelial cells. Journal of Biomechanics 35, 177–187.

Darling, E.M., Topel, M., Zauscher, S., Vail, T.P., Guilak, F., 2008. Viscoelastic properties of human mesenchymally-derived stem cells and primary osteoblasts, chondrocytes, and adipocytes. Journal of Biomechanics 41, 454–464.

Deshpande, V.S., McMeeking, R.M., Evans, A.G., 2007. A model for the contractility of the cytoskeleton including the effects of stress-fibre formation and dissociation. Proceedings of the Royal Society A: Mathematical, Physical and Engineering Science 463, 787–815.

Deshpande, V.S., Mrksich, M., McMeeking, R.M., Evans, A.G., 2008. A bio-mechanical model for coupling cell contractility with focal adhesion formation. Journal of the Mechanics and Physics of Solids 56, 1484–1510.

Engler, A.J., Sen, S., Sweeney, H.L., Discher, D.E., 2006. Matrix elasticity directs stem cell lineage specification. Cell 126, 677–689.

Franke, R.P., Grafe, M., Schnittler, H., Seiffge, D., Mittermayer, C., Drenckhahn, D., 1984. Induction of human vascular endothelial stress fibers by fluid shear-stress. Nature 307, 648–649.

Ferko, M.C., Bhatnagar, A., Garcia, M.B., Butler, P.J., 2007. Finite-element stress analysis of a multicomponent model of sheared and focally-adhered endothelial cells. Annals of Biomedical Engineering 35, 208–223.

Freeman, P.M., Natarajan, R.N., Kimura, J.H., Andriacchi, T.P., 1994. Chondrocyte cells respond mechanically to compressive loads. Journal of Orthopaedic Research 12, 311–320.

Goffin, J.M., Pittet, P., Csucs, G., Lussi, J.W., Meister, J.J., Hinz, B., 2006. Focal adhesion size controls tension-dependent recruitment of alpha-smooth muscle actin to stress fibers. Journal of Cell Biology 172, 259–268.

Haider, M.A., Guilak, F., 2002. An axisymmetric boundary integral model for assessing elastic cell properties in the micropipette aspiration contact problem. Journal of Biomechanical Engineering 124, 586–595.

Hotulainen, P., Lappalainen, P., 2006. Stress fibers are generated by two distinct actin assembly mechanisms in motile cells. The Journal of Cell Biology 173, 383–394.

Houben, F., Ramaekers, F.C.S., Snoeckx, L.H.E.H., Broers, J.L.V., 2007. Role of nuclear lamina-cytoskeleton interactions in the maintenance of cellular strength. Biochimica et Biophysica Acta (BBA)—Molecular Cell Research 1773, 675–686.

Janmey, P.A., Tee, S.Y., Fu, J.P., Chen, C.S., 2011. Cell shape and substrate rigidity both regulate cell stiffness. Biophysical Journal 100, L25–L27.

Jones, W.R., Ting-Beall, H.P., Lee, G.M., Kelley, S.S., Hochmuth, R.M., Guilak, F., 1999. Alterations in the Young's modulus and volumetric properties of chondrocytes isolated from normal and osteoarthritic human cartilage. Journal of Biomechanics 32, 119–127.

Kaunas, R., Hsu, H.J., 2009. A kinematic model of stretch-induced stress fiber turnover and reorientation. Journal of Theoretical Biology 257, 320–330.

Khatau, S.B., Hale, C.M., Stewart-Hutchinson, P.J., Patel, M.S., Stewart, C.L., Searson, P.C., Hodzic, D., Wirtz, D., 2009. A perinuclear actin cap regulates nuclear shape. Proceedings of the National Academy of Sciences 106, 19017–19022.

Kolega, J., 1986. Effects of mechanical tension on protrusive activity and microfilament and intermediate filament organization in an epidermal epithelium moving in culture. Journal of Cell Biology 102, 1400–1411.

Lulevich, V., Zink, T., Chen, H.-Y., Liu, F.-T., Liu, G.-Y., 2006. Cell mechanics using atomic force microscopy-based single-cell compression. Langmuir 22, 8151–8155.

McGarry, J.P., 2009. Characterization of cell mechanical properties by computational modeling of parallel plate compression. Annals of Biomedical Engineering 37, 2317–2325.

McGarry, J.P., Fu, J., Yang, M.T., Chen, C.S., McMeeking, R.M., Evans, A.G., Deshpande, V.S., 2009. Simulation of the contractile response of cells on an array of micro-posts. Philosophical Transactions of the Royal Society a—Mathematical Physical and Engineering Sciences 367, 3477–3497.

McGarry, J.P., McHugh, P.E., 2008. Modelling of in vitro chondrocyte detachment. Journal of the Mechanics and Physics of Solids 56, 1554–1565.

Mohrdieck, C., Wanner, A., Roos, W., Roth, A., Sackmann, E., Spatz, J.P., Arzt, E., 2005. A theoretical description of elastic pillar substrates in biophysical experiments. ChemPhysChem 6, 1492–1498.

Naumanen, P., Lappalainen, P., Hotulainen, P., 2008. Mechanisms of actin stress fibre assembly. Journal of Microscopy 231, 446–454.

Nguyen, B.V., Wang, Q.G., Kuiper, N.J., El Haj, A.J., Thomas, C.R., Zhang, Z., 2010. Biomechanical properties of single chondrocytes and chondrons determined by micromanipulation and finite-element modelling. Journal of The Royal Society Interface 7, 1723–1733.

Oakes, P.W., Beckham, Y., Stricker, J., Gardel, M.L., 2012. Tension is required but not sufficient for focal adhesion maturation without a stress fiber template. The Journal of Cell Biology 196, 363–374.

Ofek, G., Dowling, E.P., Raphael, R.M., McGarry, J.P., Athanasiou, K.A., 2009a. Biomechanics of single chondrocytes under direct shear. Biomechanics and Modeling in Mechanobiology.

Ofek, G., Natoli, R.M., Athanasiou, K.A., 2009b. In situ mechanical properties of the chondrocyte cytoplasm and nucleus. Journal of Biomechanics 42, 873–877.

Ofek, G., Dowling, E.P., Raphael, R.M., McGarry, J.P., Athanasiou, K.A., 2009a. Biomechanics of single chondrocytes under direct shear. Biomechanics and Modeling in Mechanobiology 9, 153–162 http://dx.doi.org/10.1007/s10237-009-0166-1.

Or-Tzadikario, S., Gefen, A., 2011. Confocal-based cell-specific finite element modeling extended to study variable cell shapes and intracellular structures: the example of the adipocyte. Journal of Biomechanics 44, 567–573.

Pajerowski, J.D., Dahl, K.N., Zhong, F.L., Sammak, P.J., Discher, D.E., 2007. Physical plasticity of the nucleus in stem cell differentiation. Proceedings of the National Academy of Sciences USA 104, 15619–15624.

Pathak, A., Deshpande, V.S., McMeeking, R.M., Evans, A.G., 2008. The simulation of stress fibre and focal adhesion development in cells on patterned substrates. Journal of the Royal Society Interface 5, 507–524.

Peeters, E.A., Oomens, C.W., Bouten, C.V., Bader, D.L., Baaijens, F.P., 2005. Viscoelastic properties of single attached cells under compression. Journal of Biomechanical Engineering 127, 237–243.

Peeters, E.A.G., Bouten, C.V.C., Oomens, C.W.J., Bader, D.L., Snoeckx, L.H.E.H., Baaijens, F.P.T., 2004. Anisotropic, three-dimensional deformation of single attached cells under compression. Annals of Biomedical Engineering 32, 1443–1452.

Potter, D.A., Tirnauer, J.S., Janssen, R., Croall, D.E., Hughes, C.N., Fiacco, K.A., Mier, J.W., Maki, M., Herman, I.M., 1998. Calpain regulates actin remodeling during cell spreading. Journal of Cell Biology 141, 647–662.

Roberts, S.R., Knight, M.M., Lee, D.A., Bader, D.L., 2001. Mechanical compression influences intracellular Ca^{2+} signaling in chondrocytes seeded in agarose constructs. Journal of Applied Physiology 90, 1385–1391.

Rowat, A.C., Foster, L.J., Nielsen, M.M., Weiss, M., Ipsen, J.H., 2005. Characterization of the elastic properties of the nuclear envelope. Journal of the Royal Society Interface 2, 63–69.

Sato, K., Adachi, T., Yasuhito, S., 2006. Local disassembly of actin stress fibers induced by selected release of intracellular tension in osteoblastic cell. Journal of Biomechanical Science and Engineering 1, 204–214.

Schober, M., Raghavan, S., Nikolova, M., Polak, L., Pasolli, H.A., Beggs, H.E., Reichardt, L.F., Fuchs, E., 2007. Focal adhesion kinase modulates tension signaling to control actin and focal adhesion dynamics. The Journal of Cell Biology 176, 667–680.

Shieh, A., Koay, E., Athanasiou, K., 2006. Strain-dependent recovery behavior of single chondrocytes. Biomechanics and Modeling in Mechanobiology 5, 172–179.

Storm, C., Pastore, J.J., MacKintosh, F.C., Lubensky, T.C., Janmey, P.A., 2005. Nonlinear elasticity in biological gels. Nature 435, 191–194.

Thoumine, O., Cardoso, O., Meister, J.J., 1999. Changes in the mechanical properties of fibroblasts during spreading: a micromanipulation study. European Biophysics Journal with Biophysics Letters 28, 222–234.

Thoumine, O., Ott, A., 1997. Time scale dependent viscoelastic and contractile regimes in fibroblasts probed by microplate manipulation. Journal of Cell Science 110, 2109–2116.

Trickey, W.R., Baaijens, F.P.T., Laursen, T.A., Alexopoulos, L.G., Guilak, F., 2006. Determination of the Poisson's ratio of the cell: recovery properties of chondrocytes after release from complete micropipette aspiration. Journal of Biomechanics 39, 78–87.

Vernerey, F.J., Farsad, M., 2011. A constrained mixture approach to mechano-sensing and force generation in contractile cells. Journal of the Mechanical Behavior of Biomedical Materials 4, 1683–1699.

Warshaw, D.M., Desrosiers, J.M., Work, S.S., Trybus, K.M., 1990. Smooth muscle myosin cross-bridge interactions modulate actin filament sliding velocity in vitro. Journal of Cell Biology 111, 453–463.

Weafer, P.P., Ronan, W., Jarvis, S.P., McGarry, J.P., Experimental and computational investigation of the role of stress fiber contractility in the resistance of osteoblasts to compression. Bulletin of Mathematical Biology, submitted for publication.